scientific reports

Check for updates

OPEN

Specific heat analyses on optical-phonon-derived uniaxial negative thermal expansion system $TrZr_2$ (tr = fe and $Co_{1-x}Ni_x$)

Yuto Watanabe[1], Ceren Tayran[2,3]✉, Md. Riad Kasem[1], Aichi Yamashita[1], Mehmet Çakmak[4,5], Takayoshi Katase[6] & Yoshikazu Mizuguchi[1]✉

A large uniaxial negative thermal expansion (NTE) along the *c*-axis has recently been observed in the transition metal (*Tr*) zirconides $TrZr_2$ with a tetragonal $CuAl_2$-type structure. A recent study on $FeZr_2$ [M. Xu et al., *Nat. Commun.* 14, 4439 (2023)] suggests that optical phonons play a critical role in inducing the NTE along the *c*-axis. In this study, we investigate the thermophysical properties of $TrZr_2$ compounds (Tr = Fe and $Co_{1-x}Ni_x$(x = 0, 0.2, 0.4, 0.6, 0.8, 1)) using specific heat measurements, sound velocity data, and theoretical phonon calculations to achieve our aim of clarifying the contribution of optical phonons to the uniaxial NTE along the *c*-axis observed in both $FeZr_2$ and $CoZr_2$. We found that $FeZr_2$ shows a lattice-specific heat peak structure at 8.90 meV, which corresponds to optical phonon energy with a high population of negative Grüneisen parameter along the *c*-axis in the phonon dispersion curves in $FeZr_2$. In an examination of a chemical substitution effect on the $Co_{1-x}Ni_xZr_2$, we found that the lattice-specific heat peak structure disappeared for $x \geq 0.4$ and the oscillator intensity decreased. Phonon calculations revealed the existence of low-energy optical phonon branches at the Γ point for $CoZr_2$ and $FeZr_2$ with uniaxial NTE along the *c*-axis. However, the low-energy phonon branches were not found in $NiZr_2$ with uniaxial positive thermal expansion along the *c*-axis. The increase in phonon density of states near the above optical phonon energy in $CoZr_2$ and $FeZr_2$ is consistent with the lattice-specific heat analyses, and we propose that low-energy optical phonons are essential for the exhibiting of uniaxial NTE along the *c*-axis in $TrZr_2$.

Keywords Superconductivity, Specific heat, Negative thermal expansion, DFT calculation

Negative thermal expansion (NTE) materials that contract upon heating have the potential to tune the thermal expansion of materials. Control of thermal expansion property of materials is important for producing high-performance devices because even such a small expansion can degrade the performance of devices in modern advanced technology[1]. ZrW_2O_8 is a typical NTE material, and the striking feature is the wide temperature range (0.3 K < T < 1050 K) NTE caused by the unique low-energy phonon mode[2–4]. The low-energy phonon modes propagate without distorting constituent units, ZrO_6 octahedra and WO_4 tetrahedra, which are known as Rigid Unit Modes (RUMs). The mechanism of NTE in ZrW_2O_8 is based on the RUMs which cause collective rotations of ZrO_6 octahedra and WO_4tetrahedra[5]. Another typical NTE mechanism is related to electronic structure transition. For example, the manganese antiperovskite nitride shows sharp volume change because of the first-order antiferromagnetic transition, called as magnet volume effect[6,7]. In addition, in superconductors, NTE has been observed mostly below superconducting transition temperature (T_c), which is typically quite low. NTE phenomena in superconductors can be achieved by an evolution of the superconducting order parameter[8,9]. For NTE materials associated with electronic structure transition such as magnetic compounds and superconductors, realizing the wide-temperature range NTE is quite rare because the NTE can be realized by order-disorder phase transitions. If we could achieve volumetric zero thermal expansion with a wide temperature range in a

[1]Department of Physics, Tokyo Metropolitan University, Hachioji, Tokyo 192-0397, Japan. [2]Department of Physics, Faculty of Science, Gazi University, Ankara 06500, Turkey. [3]DIFFER–Dutch Institute for Fundamental Energy Research, De Zaale 20, Eindhoven 5612 AJ, The Netherlands. [4]Department of Photonics, Faculty of Applied Sciences, Gazi University, Ankara 06500, Turkey. [5]Photonics Application and Research Center, Gazi University, Ankara 06500, Turkey. [6]MDX Research Center for Element Strategy, International Research Frontiers Initiative, Tokyo Institute of Technology, Yokohama 226-8501, Japan. ✉email: c.tayran@gazi.edu.tr; mizugu@tmu.ac.jp

superconductor, it is useful for superconductor devices or junctions with nano-scale structure or robustness to heat cycles between quite low temperatures and room temperature.

Recently, we revealed that the $CoZr_2$ superconductor (T_c ~ 5 K) shows uniaxial NTE along the *c*-axis in a wide temperature range (7 K < *T* < 573 K)[10]. Note that the volume itself expands upon heating because the *a*-axis shows the usual PTE. According to the neutron scattering experiment, there are no crystal structural transitions or magnetic ordering down to 7 K. Therefore, the cause of uniaxial *c*-axis NTE should be not related to magnetic ordering, which is in contrast to the case of the manganese antiperovskite nitride. Also, the uniaxial NTE along the *c*-axis would not be directly connected to its superconducting transition because the NTE nature can be observed from low-temperature to high-temperature regions. Therefore, we can think the uniaxial NTE along the c-axis should be driven by phonons contributing specific lattice vibration. Such materials which can balance the NTE and superconductivity are quite rare. We can fully or partially substitute the Co site with other transition metals (*Tr*) in the tetragonal $CuAl_2$-type $TrZr_2$. We succeed in tuning the uniaxial *c*-axis NTE by chemical substitution of Co by Ni[11]. The tunable uniaxial *c*-axis NTE is highly correlated with a ratio of lattice parameters *c*/*a*, large *c*/*a* (*c*/*a* > 0.84) favors leading the uniaxial *c*-axis NTE; for example, *Tr* = Co, (Fe, Co, Ni), (Fe, Co, Rh, Ir), and so on[12]. However, small *c*/*a* leads to PTE along the *c*-axis; therefore, the uniaxial *c*-axis NTE is absent for *Tr* = Ni. Based on the flexibility of control of the uniaxial *c*-axis thermal expansion nature, there are possibilities to achieve zero or near zero thermal expansion superconductors. In such a case, it would play an important role in the implementation of modern nanoscale superconducting devices such as containing Josephson junctions applied to high-speed and energy-sufficient circuits[13] because they are delicate to slight thermal expansion. To facilitate the development of materials with zero thermal expansion based on $TrZr_2$ superconductor, it is important to understand mechanisms causing the uniaxial NTE along the *c*-axis.

Figure 1 (a) shows the crystal structure of tetragonal $CuAl_2$-type $TrZr_2$. On the uniaxial NTE along the *c*-axis, the shape of a Tr_2Zr_4 octahedron unit is modified during cooling as shown in Fig. 1 (b). According to density functional theory (DFT) calculations, the presence of relatively high-frequency optical phonon modes with huge negative Grüneisen parameters is the cause of the huge uniaxial *c*-axis NTE in $FeZr_2$[14]. In $FeZr_2$, there are optical phonon modes with negative γ_c (Grüneisen parameter along the *c*-axis) which generate soft Fe-Fe bonds along the *c*-axis. Moreover, the authors observed a large thermal expansion of Fe-Zr bonds through the EXAFS (extended X-ray absorption fine structure) experiments. Based on the soft Fe-Fe bonds and strong expansion of Fe-Zr bonds, Fe-Fe bond length can easily contract to maintain stable Fe_2Zr_4 octahedra, resulting in the uniaxial NTE along the *c*-axis. Although theoretical approaches have been shown, the experimental investigation of the optical phonon modes has not been performed for $TrZr_2$. Therefore, we investigate the thermophysical properties of $TrZr_2$ compounds (*Tr* = Fe and $Co_{1-x}Ni_x$ (x = 0, 0.2, 0.4, 0.6, 0.8, 1)) using specific heat measurements, sound velocity data to achieve our aim of clarifying the contribution of optical phonons to the uniaxial NTE along the *c*-axis. Also, the experimental results are discussed in conjunction with the phonon calculation results. This study will provide a promising platform for exploring superconductors with anomalous thermal expansion nature, and understanding the mechanism of the NTE not only enriches our comprehension of $TrZr_2$ but could also inform future research in material design for specific applications such as zero thermal expansion superconductors.

Results

First, we analyze the specific heat data of $CoZr_2$, $FeZr_2$, and $NiZr_2$. The temperature dependences of the total specific heat $C(T)$ under zero field are shown in Fig. 2(a). We confirmed that values of $C(T)$ at around 300 K are close to the Dulong-Petit law value, $3nR$ = 74.8 J/K mol, where n = 3 is the number of atoms per formula unit, and $R \approx 8.31$ J/K mol is an ideal gas constant. Figure 2(b) shows the squared-temperature dependences of the total specific heat under zero field in the form of $C(T)/T$. $CoZr_2$ shows a superconducting transition at around 5 K under zero field, which is consistent with previous works on $CoZr_2$[15,16]. No bulk superconducting transition was detected by specific heat for $FeZr_2$ and $NiZr_2$ under zero field above 1.8 K. The $C(T)/T$ data between 40 $K^2 < T^2 < 100$ K^2 were fitted to $C(T)/T = \gamma + \beta T^2$, where γ and β are Sommerfeld coefficients and coefficient of phonon contribution to total specific heat, respectively. We can extract only phonon contribution to total specific heat $C_{lat}(T)$ by subtracting electronic specific heat γT from $C(T)$. Figure 2(c) shows the temperature dependences of phonon contribution to total specific heat in the form of $C_{lat}(T)/T^3$ between 7 K < *T* < 300 K for $CoZr_2$, $FeZr_2$, and $NiZr_2$. We found a peak structure (Schottky-type specific heat anomaly) in $C_{lat}(T)/T^3$ at around 20 K for $CoZr_2$ and $FeZr_2$ whereas the peak structure is absent in $NiZr_2$. The observed peak structure in $C_{lat}(T)/T^3$ for $CoZr_2$ and $FeZr_2$ would be related to the optical phonon modes which were proposed to be a possible cause of

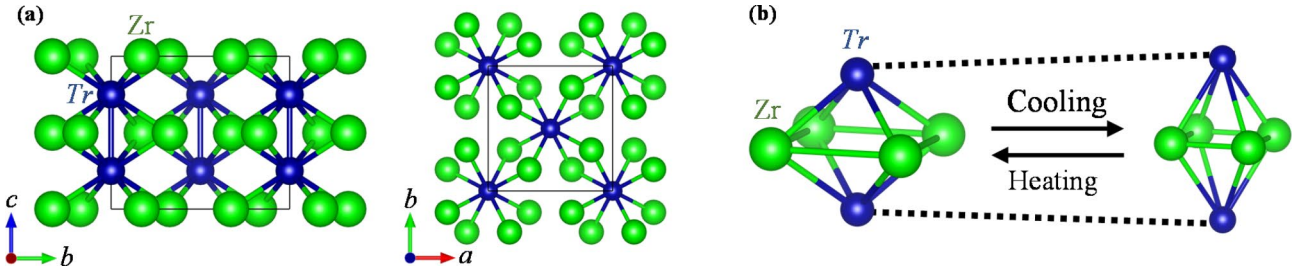


Fig. 1. Schematic images of the (**a**) crystal structure of $CuAl_2$-type $TrZr_2$ and (**b**) Tr_2Zr_4 octahedron unit.

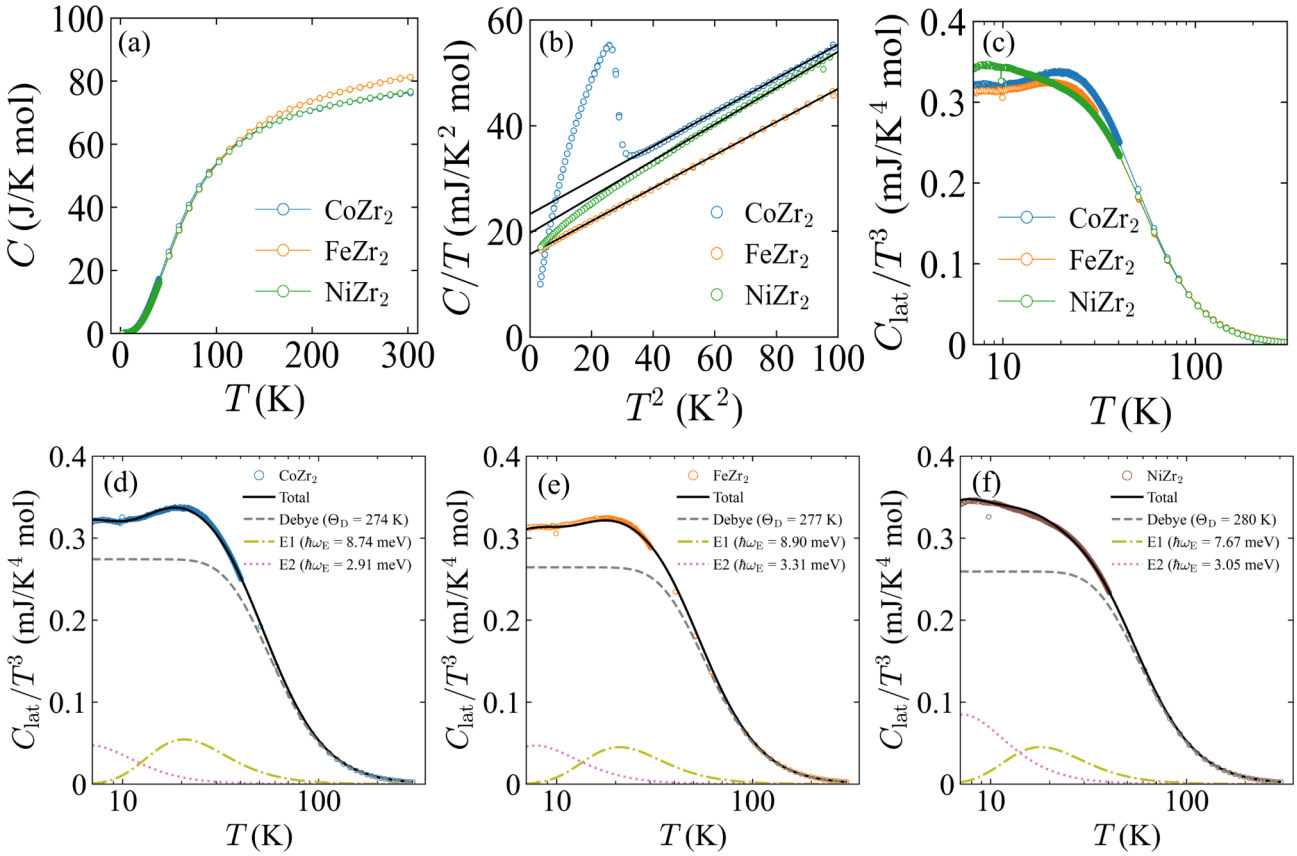


Fig. 2. (**a**) Temperature dependences of total specific heat $C(T)$ under zero field for $CoZr_2$, $FeZr_2$, and $NiZr_2$. (**b**) Squared temperature dependences of total specific heat under zero field in the form of $C(T)/T$. Solid lines are the fit of $C(T)/T = \gamma + \beta T^2$. (**c**) Temperature dependences of phonon contribution to total specific heat in the form of $C_{lat}(T)/T^3$ for $CoZr_2$, $FeZr_2$, and $NiZr_2$. (**d**–**f**) Fitting results of $C_{lat}(T)/T^3$ using a single Debye model and double Einstein models (E1 and E2) for $CoZr_2$, $FeZr_2$, and $NiZr_2$, respectively.

the uniaxial *c*-axis NTE in $FeZr_2$[14]. DFT calculations revealed that giant *c*-axis NTE observed in $FeZr_2$is mainly driven by the optical phonon branches with relatively high energy above roughly 8 meV[14]. In $FeZr_2$, the high-frequency optical phonon modes excite multiple, large, and negative γ_c; therefore, the uniaxial *c*-axis NTE is induced. $NiZr_2$ exhibits uniaxial *c*-axis PTE because the optical phonon branches with negative γ_c are absent. Therefore, we expect that the optical phonon branches with negative γ_c are present for $CoZr_2$ as in $FeZr_2$ and contribute to the emergence of the uniaxial *c*-axis NTE in a wide temperature range[10].

To discuss the optical phonon contributions to the uniaxial NTE along the *c*-axis, we analyze the $C_{lat}(T)/T^3$ data using a model based on the combination with the Debye and Einstein models. Related analyses have been attempted in phonon-driven flexible network NTE materials for instance ZrW_2O_8[3]. From neutron scattering experiments, the low-energy phonon modes with 1.5–8.5 meV are suggested to play an important role in NTE[4] for ZrW_2O_8, and the low-energy phonon modes were quantitively analyzed by the Einstein model reflecting optical phonon branches[3]. In our analysis for $CoZr_2$, $FeZr_2$, and $NiZr_2$, we adopt a model with a single Debye model and double Einstein models to obtain quantitative insight into optical phonon related to *c*-axis thermal expansion. Debye model $C_D(T)$ and Einstein model $C_E(T)$ per atom in J/K mol unit are expressed in the following equations.

$$C_D(T) = 9R\left(\frac{T}{\Theta_D}\right)^3 \int_0^{\frac{\Theta_D}{T}} \frac{x^4 e^x}{(e^x - 1)^2} dx,$$

$$C_E(T) = 3R\left(\frac{\Theta_E}{T}\right)^2 \frac{\exp\left(\frac{\Theta_E}{T}\right)}{\left[\exp\left(\frac{\Theta_E}{T}\right) - 1\right]^2},$$

where Θ_D and Θ_E are Debye temperature and Einstein temperature, respectively. In the Debye model, it assumes a constant sound velocity and phonon density of states proportions to the square of phonon angular frequency. On the other hand, in the Einstein models, the phonon density of states is expressed with a delta function centered by a specific phonon angular frequency. Therefore, the Debye model and Einstein model correspond

to proximate expression for acoustic phonon contribution and optical phonon contribution, respectively. Based on the features of the Debye model and Einstein model, the combination model tries to explain the total phonon density of states (DOS) by a single Debye function, but the Schottky-type specific heat contribution is fitted using the Einstein functions. The number of atoms in the formula unit is 3 for $CoZr_2$, $FeZr_2$, and $NiZr_2$; therefore, in our model, phonon contribution to total specific heat is described as $C_{lat}(T) = n_D C_D(T) + n_{E1} C_E(T) + n_{E2} C_E(T)$ with the summation rule of $n_D + n_{E1} + n_{E2} = 3$ where n is the oscillator strength that is the parameter of the weight of each model related to the assumed partial DOS. We determined the parameters of oscillator strength (n_D, n_{E1}, and n_{E2}), Θ_D, and Θ_E as most explain the $C_{lat}(T)/T^3$ data. The fitting results of $C_{lat}(T)/T^3$ for $CoZr_2$, $FeZr_2$, and $NiZr_2$ are shown in Fig. 2(d), 2(e), and 2(f), respectively. The fitting parameters are summarized in Table 1. The Θ_D values were estimated through the Debye modes as 274 K ($n_D = 2.8898$) for $CoZr_2$, 277 K ($n_D = 2.9019$) for $FeZr_2$, and 280 K ($n_D = 2.9331$) for $NiZr_2$. We can consider the peak structures of $C_{lat}(T)/T^3$ observed in $CoZr_2$ and $FeZr_2$ are responsible for E1 modes with $\hbar\omega_{E1} = 8.74$ meV ($n_{E1} = 0.1068$) and $\hbar\omega_{E1} = 8.90$ meV ($n_{E1} = 0.0931$), respectively. The fitting revealed that the estimated E1 mode energy of $FeZr_2$ corresponds to the optical phonon energy which plays an important role in emerging uniaxial c-axis NTE suggested by DFT calculations[14]. We also confirmed that the E1 mode energy and oscillator strength of $CoZr_2$ are comparable with those of $FeZr_2$. Therefore, the uniaxial c-axis NTE in $CoZr_2$ and $FeZr_2$ would be attributed to the optical phonon modes corresponding to the E1 modes. For analysis of $NiZr_2$, we found E1 mode energy $\hbar\omega_{E1} = 7.67$ meV is close to that of $CoZr_2$ and $FeZr_2$; however, $n_{E1} = 0.0598$ is clearly smaller than that of $CoZr_2$ and $FeZr_2$. Therefore, the phonon DOS of the E1 mode for $NiZr_2$ is not dominant to the $C_{lat}(T)$, and the fitting result is consistent with the absence of optical phonon branches with negative γ_c leading the uniaxial c-axis NTE[14]. The Einstein mode with lower energy (E2) is considered to hardly contribute to the emergence of NTE for $CoZr_2$, $FeZr_2$, and $NiZr_2$ because the oscillator strength is lowest for others. According to the phonon dispersion curves calculation of $FeZr_2$ performed by Xu et al., [Xu, M. et al., *Nat. Commun.* **14**, 4439 (2023).] atomic vibration modes on optical phonon branches with negative γ_c (Grüneisen parameter along the c-axis) represent the distortion of Fe_2Zr_4 units. For instance, they revealed that in the vibration model at the X point, the Zr atoms in the four corners of Fe_2Zr_4 units inclined to centrifugal motions, which contribute to uniaxial NTE along the c-axis. We expect that other $TrZr_2$ compounds exhibiting uniaxial NTE along the c-axis also have very similar vibration modes because we observed the optical phonon modes relating to the uniaxial NTE along the c-axis. The optical phonons contribute to the uniaxial NTE along the c-axis through their unique vibrational modes and interactions with other phonon types. The anharmonicity of these modes, softening at elevated temperatures, and their coupling with acoustic modes are critical mechanisms that enable certain materials to exhibit NTE. To understand these mechanisms, we would need to look closely at how atoms in the material vibrate and how these vibrations affect the material's overall behavior when it is heated or cooled in future works.

Furthermore, we analyze specific heat data of the $Co_{1-x}Ni_xZr_2$ ($x = 0.2$, 0.4, 0.6, 0.8) solid-solution system and evaluate optical phonon contributions. We recently succeeded in controlling (switching) thermal expansion along the c-axis by Ni substitution for Co site in $CoZr_2$. With increasing Ni amount, the uniaxial c-axis NTE gradually changes to uniaxial c-axis PTE[11]. Based on the success of controlling the thermal expansion along the c-axis by chemical substitution, we expect that the peak structure of $C_{lat}(T)/T^3$ observed in $CoZr_2$ gradually disappears with increasing Ni amount. Figure 3 shows the fitting results of $C_{lat}(T)/T^3$ for $Co_{1-x}Ni_xZr_2$ ($x = 0$, 0.2, 0.4, 0.6, 0.8, 1) using the similar model with single Debye model and double Einstein models. The fitting parameters are summarized in Table 2. The clear peak structures of $C_{lat}(T)$ were observed in $CoZr_2$ ($x = 0$) and $Co_{0.8}Ni_{0.2}Zr_2$ ($x = 0.2$) whereas the peak structures were absent in $x = 0.4$, 0.6, 0.8, and 1. The observation results of $C_{lat}(T)/T^3$ are consistent with the change of uniaxial c-axis thermal expansion from NTE to PTE by Ni substitution because the uniaxial c-axis NTE region of $Co_{1-x}Ni_xZr_2$ system mainly is $x = 0$–0.3[11]. The oscillator strength of the E1 mode (n_{E1}) gradually decreased with increasing Ni amount, which indicates the contribution of the E1 mode related to the uniaxial c-axis NTE to $C_{lat}(T)$ becomes smaller. We also found the E1

$CoZr_2$		
Mode	**Energy**	**Oscillator strength**
Debye	274 K	2.8898
E1	8.74 meV	0.1068
E2	2.91 meV	0.0034
$FeZr_2$		
Mode	**Energy**	**Oscillator strength**
Debye	277 K	2.9019
E1	8.90 meV	0.0931
E2	3.31 meV	0.0050
$NiZr_2$		
Mode	**Energy**	**Oscillator strength**
Debye	280 K	2.9331
E1	7.67 meV	0.0598
E2	3.05 meV	0.0071

Table 1. Fitting parameters of $C_{lat}(T)/T^3$ for $CoZr_2$, $FeZr_2$, and $NiZr_2$.

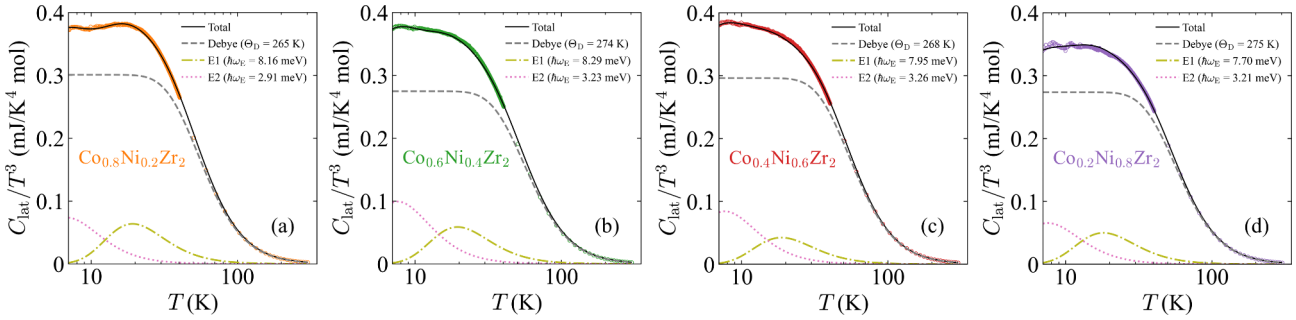


Fig. 3. Fitting results of $C_{lat}(T)/T^3$ using a single Debye model and double Einstein models (E1 and E2) for (**a**) $Co_{0.8}Ni_{0.2}Zr_2$ ($x=0.2$), (**b**) $Co_{0.6}Ni_{0.4}Zr_2$ ($x=0.4$), (**c**) $Co_{0.4}Ni_{0.6}Zr_2$ ($x=0.6$), and (**d**) $Co_{0.2}Ni_{0.8}Zr_2$ ($x=0.8$).

$CoZr_2$ ($x=0$)			$Co_{0.8}Ni_{0.2}Zr_2$ ($x=0.2$)		
Mode	**Energy**	**Oscillator strength**	**Mode**	**Energy**	**Oscillator strength**
Debye	274 K	2.8898	Debye	265 K	2.8932
E1	8.74 meV	0.1068	E1	8.16 meV	0.1015
E2	2.91 meV	0.0034	E2	2.91 meV	0.0053
$Co_{0.6}Ni_{0.4}Zr_2$ ($x=0.4$)			$Co_{0.4}Ni_{0.6}Zr_2$ ($x=0.6$)		
Mode	**Energy**	**Oscillator strength**	**Mode**	**Energy**	**Oscillator strength**
Debye	274 K	2.8921	Debye	268 K	2.92896
E1	8.29 meV	0.0981	E1	7.95 meV	0.06248
E2	3.23 meV	0.0098	E2	3.26 meV	0.00856
$Co_{0.2}Ni_{0.8}Zr_2$ ($x=0.8$)			$NiZr_2$ ($x=1$)		
Mode	**Energy**	**Oscillator strength**	**Mode**	**Energy**	**Oscillator strength**
Debye	275 K	2.92682	Debye	280 K	2.9331
E1	7.70 meV	0.06680	E1	7.67 meV	0.0598
E2	3.21 meV	0.00638	E2	3.05 meV	0.0071

Table 2. Fitting parameters of $C_{lat}(T)/T^3$ for $Co_{1-x}Ni_xZr_2$ ($x=0$, 0.2, 0.4, 0.6, 0.8, and 1).

mode energy tends to decrease with increasing Ni concentration, which means Ni substitution cause phonon softening. Phonon softening in $TrZr_2$ plays a key role in causing uniaxial NTE along the *c*-axis. As temperature increases, certain optical phonons (vibrations) soften, meaning their frequencies decrease, allowing atoms to vibrate more freely. This is due to changes in atomic interactions, called anharmonic effects. The softer phonons lower the energy needed for atoms to shift, especially along the *c*-axis, leading to a contraction of the lattice in that direction. As a result, the atoms move closer together rather than further apart. This behavior becomes more stable at higher temperatures, causing the material to shrink along the *c*-axis instead of expanding. In the future, direct observation of the phonon dispersion curve by inelastic neutron scattering should be important to discuss how chemical substitution actually affects the phonon softening. Moreover, a high-pressure inelastic neutron scattering experiment may be effective because we can estimate the Grüneisen parameter by softening the phonon spectrum under pressure, and then we can elucidate which phonon energy regions are related to the anomalous thermal expansion on the $TrZr_2$ system. In the discussion part, we show phonon calculation results and discuss the possible mechanisms of the emergence of the *c*-axis NTE in $TrZr_2$.

In addition, we measured transverse (v_t) and longitudinal (v_l) sound velocities for $CoZr_2$ and $NiZr_2$. The sound velocities at room temperature were $v_t = 1736$ m s^{-1} (1801 m s^{-1}) and $v_l = 2968$ m s^{-1} (4300 m s^{-1}) for $CoZr_2$ ($NiZr_2$). An average sound velocity v_s can be calculated using the following equation:

$$v_s = \left[\frac{1}{3}\left(\frac{2}{v_t^3}+\frac{1}{v_l^3}\right)\right]^{-\frac{1}{3}}.$$

We obtained $v_s = 1925$ m s^{-1} and 2037 m s^{-1} for $CoZr_2$ and $NiZr_2$, respectively. From obtained v_s values, we can calculate Θ_D values of $CoZr_2$ and $NiZr_2$ by the following equation:

$$\Theta_D = \frac{\hbar}{k_B}\left(\frac{6\pi^2 N}{V}\right)^{\frac{1}{3}} v_s,$$

where $\hbar \approx 1.05\times10^{-34}$ J s is a reduced Planck constant, $k_B \approx 1.38\times10^{-23}$ J K^{-1} is a Boltzmann constant, and $N=12$ is the number of atoms in the unit cell. $V \approx 226.98$ Å^3 (224.87 Å^3) is a calculated volume of the unit cell

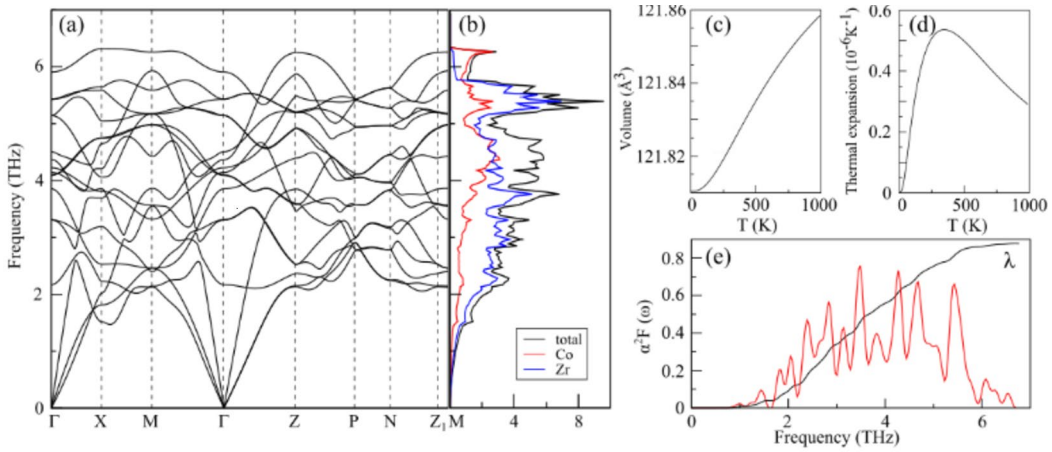


Fig. 4. The calculated (**a**) phonon dispersion curves, (**b**) total and partial phonon density of states, (**c**) Volume-temperature and (**d**) thermal expansion coefficient-temperature relations, and (**e**) Eliashberg spectral function $F(\omega)$ and integrated electron-phonon coupling constant λ of $CoZr_2$.

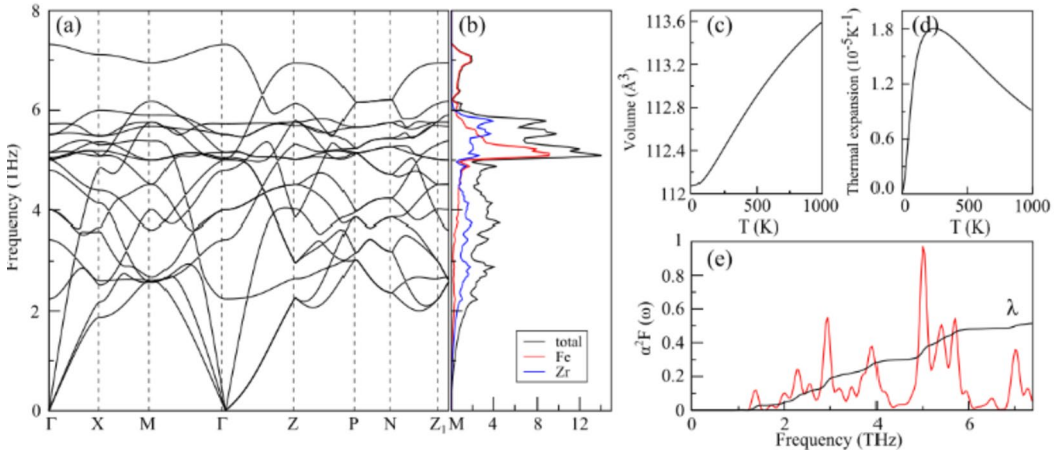


Fig. 5. The calculated (**a**) phonon dispersion curves, (**b**) total and partial phonon density of states, (**c**) Volume-temperature and (**d**) thermal expansion coefficient-temperature relations, and (**e**) Eliashberg spectral function $F(\omega)$ and integrated electron-phonon coupling constant λ of $FeZr_2$.

by Rietveld refinement for $CoZr_2$ ($NiZr_2$). The calculated Θ_D values were 215 K and 228 K for $CoZr_2$ and $NiZr_2$, respectively; the trend agrees with the estimated Θ_D values from the specific heat data analysis.

Discussion

From the specific heat analyses, we revealed that the optical-phonon (~ 8.7 meV) contributions to C_{lat} in $CoZr_2$ are weakened by Ni substitution, and the uniaxial *c*-axis NTE is suppressed and switches to uniaxial *c*-axis PTE by Ni substitution in $Co_{1-x}Ni_xZr_2$[11]. Here, we discuss the experimental results by comparing them with phonon calculations of $CoZr_2$, $FeZr_2$, and $NiZr_2$. The connection implies that conducting phonon calculations is essential in understanding the effects of introducing Ni into the $Co_{1-x}Ni_xZr_2$ compound. The phonon dispersion within $CoZr_2$, $FeZr_2$, and $NiZr_2$, each characterized by a primitive cell comprising six atoms and a total of eighteen phonon branches, consisting of three acoustic and fifteen optical branches. Through computations across high symmetry points in the Brillouin zone (as depicted in Fig. 4 (a) for $CoZr_2$, Fig. 5 (a) for $FeZr_2$, and Fig. 6(a) for $NiZr_2$), we confirm the compounds' dynamical stability, observing an absence of negative frequencies. The crossing between acoustic and optical modes is notably observed at the Γ—X—M—Γ—Z—P—N—Z1—M high symmetry points within the Brillouin zone for all three compounds. While the highest frequencies of the optical mode vary, with $CoZr_2$ and $NiZr_2$ surpassing 6 THz and $FeZr_2$ exceeding 7 THz, the lowest optical phonon branches are consistently found at the Γ point, with the highest at different symmetry points. This results in the appearance of clear peaks in phonon density of states (PDOS), and the larger optical PDOS in $CoZr_2$ and $FeZr_2$ than in $NiZr_2$ is consistent with the specific heat analyses. Additionally, the highest acoustic modes vary in location between the Γ and Z points. Analysis of the total and partial phonon density of states

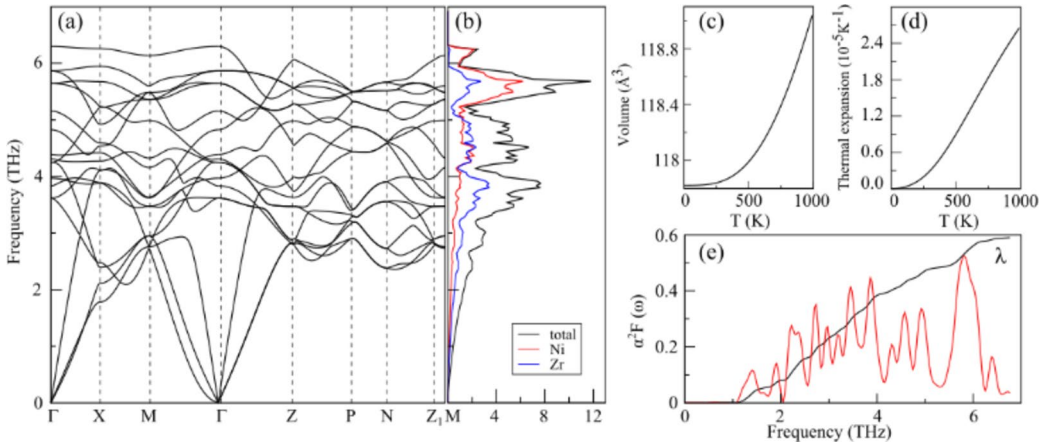


Fig. 6. The calculated (**a**) phonon dispersion curves, (**b**) total and partial phonon density of states, (**c**), Volume-temperature and (**d**) thermal expansion coefficient-temperature relations, and (**e**) Eliashberg spectral function $F(\omega)$ and integrated electron-phonon coupling constant λ of $NiZr_2$.

Compounds	λ	T_c (K) Calc.	T_c (K) Expt.	Θ_D (K) Calc.	Θ_D (K) Expt.
$CoZr_2$	0.87	5.87	5.5[17], 5.0[18], 6.3[19]	232	274
$FeZr_2$	0.51	0.81	0.17[17,20]	207	277
$NiZr_2$	0.59	1.56	1.6, 1.52[17,19]	267	280

Table 3. Computed λ, T_c and Θ_D values for $CoZr_2$, $FeZr_2$, and $NiZr_2$. For T_c calculation, $\mu^* = 0.16$ is taken. Experimental Θ_D values are taken from specific heat analyses.

across these materials, depicted in respective figs. (Fig. 4 (b) for $CoZr_2$, Fig. 5 (b) for $FeZr_2$, and Fig. 6 (b) for $NiZr_2$), reveals distinct contributions, with Zr primarily contributing to low frequencies, while Co dominates in $CoZr_2$ and Fe alongside Zr in $FeZr_2$ at higher frequencies due to their significant atomic mass differences. These findings shed light on the diverse phonon behaviors in these compounds, providing valuable insights into their dynamic properties and potential applications in various fields. The volume-temperature relationships and thermal expansion behaviors for $CoZr_2$ are illustrated in Fig. 4(c-d), while for $FeZr_2$ and $NiZr_2$, these can be found in Fig. 5(c-d) and Fig. 6(c-d), respectively. Concerning the variation of volume with temperature, an intriguing trend emerges. In the case of $CoZr_2$, we note a negative slope of thermal expansion between 250 K and 500 K, indicating the suppression of thermal expansion as temperature increases. This trend is mirrored in $FeZr_2$, suggesting a similar behavior. However, $NiZr_2$ exhibits larger thermal expansion coefficients and a monotonous increase in thermal expansion coefficient, consistent with the presence of normal PTE in $NiZr_2$. These experimental findings align well with our expectations and contribute to our understanding of the distinct thermal expansion properties exhibited by these compounds. The transition metals (Fe, Co, Ni) in $TrZr_2$ compounds play a crucial role in altering the phonon spectrum, which directly affects the material's thermal expansion behavior. Each metal has different atomic masses and bonding characteristics, leading to variations in how the atoms vibrate (phonon modes). For instance, Co and Fe contribute to lower-frequency optical phonon modes that can soften and lead to uniaxial NTE along the *c*-axis. However, when Ni is substituted, these low-frequency modes weaken, and the material starts to show positive thermal expansion. This is because Ni, having different bonding characteristics, changes the vibrational behavior of the lattice, making it harder for the atoms to move closer together as the temperature rises. Thus, the type of transition metal used modifies the lattice dynamics, either supporting or preventing NTE in the material. Actually, *Tr* elements substitutions for $TrZr_2$ also play a role in changing the nature of uniaxial thermal expansion along the *c*-axis. We can modify the lattice constants ratio, *c*/*a* by *Tr* substitutions, and we can control the coefficient of thermal expansion along the c-axis with a *c*/*a* value at room temperature. In other words, large *c*/*a* (> 0.84) favors leading the uniaxial NTE along the *c*-axis[12]. We confirmed that $FeZr_2$, $CoZr_2$, and $Co_{0.8}Ni_{0.2}Zr_2$, which are exhibiting uniaxial NTE along the *c*-axis have relatively large *c*/*a* at room temperature as shown in figs S1(c) and (d).

Finally, we calculate the T_c of the materials using the calculation results. Figures 4(e), 5(e), and 6(e) show a detailed analysis of $\alpha^2F(\omega)$ and the integrated electron-phonon coupling constant λ across different frequencies, accounting for an effective Coulomb repulsion of $\mu^* = 0.16$. This analysis continues in Table 3, where we record the logarithmically averaged frequency ω_{log}, the electron-phonon coupling constant, and the resulting T_c. Remarkably, our computed T_c values for these materials exhibit a good agreement with experimental observations, emphasizing the strength and precision of our theoretical framework in revealing the complex mechanisms that govern superconductivity in these materials. An analysis of the Θ_D for $CoZr_2$, $FeZr_2$, and $NiZr_2$ was conducted, providing theoretical values of 232 K, 207 K, and 267 K, respectively. The trend that the highest Θ_D is observed in $NiZr_2$ is consistent with experimental Θ_D values shown above.

In summary, the physical properties of the polycrystalline samples of $CuAl_2$-type $TrZr_2$ have been studied experimentally (specific heat and sound velocity experiments) and theoretically (phonon calculations) to discuss the possible causes of *c*-axis NTE in $CoZr_2$ and $FeZr_2$. From analyses of C_{lat}, we found that Ni substitution results in a systematic decrease in oscillator strength for the Einstein modes with 8.74 meV ($CoZr_2$). From phonon calculations, the low-energy optical phonon branches at the Γ point were observed for $CoZr_2$ and $FeZr_2$ with *c*-axis NTE, but not in $NiZr_2$ with PTE. The enhancement of PDOS near the optical phonon energy in $CoZr_2$ and $FeZr_2$ is consistent with the specific heat analyses. We propose the importance of the low-energy optical phonons to the emergence of *c*-axis NTE in $TrZr_2$. The validity of the phonon calculations was confirmed by calculating the T_c of the materials.

Methods

Experimental methods

Polycrystalline samples of $FeZr_2$ and $Co_{1-x}Ni_xZr_2$ ($x=0$, 0.2, 0.4, 0.6, 0.8, 1) were synthesized through arc melting using Fe powder (Kojundo Chemical 99.9%), Co rods (Nilaco Corporation 99.98%), Ni wires (Nilaco Corporation 99%), and Zr plates (Nilaco Corporation 99.2%). Pelletized Fe powders and Co, Ni, and Zr solids were weighed as stoichiometric ratios. The atmospheric gas inside the arc furnace was replaced 3 times by pure Ar gas. Then, we started to melt the prepared pellet and the solids in the Ar atmosphere. A Ti ingot was used to absorb residual O_2 gas before synthesis. The samples were melted several times and turned over at each melting to improve homogeneity.

X-ray diffraction (XRD) patterns of the obtained polycrystalline samples were collected by θ-2θ method with Cu-Kα radiation on a Miniflex-600 (RIGAKU) diffractometer equipped with a high-resolution semiconductor detector D/tex-Ultra. The crystal structure of $FeZr_2$ and $Co_{1-x}Ni_xZr_2$ ($x=0$, 0.2, 0.4, 0.6, 0.8, 1) were confirmed as $CuAl_2$-type tetragonal structure (*I*4/*mcm*) by refining the XRD patterns using RIETAN-FP[21]. The obtained XRD patterns are shown in fig. S1(a) of the supplemental material. We confirmed that Ni was successfully substituted in the $Co_{1-x}Ni_xZr_2$ ($x=0$, 0.2, 0.4, 0.6, 0.8, 1) system because lattice constants *a* and *c* were systematically changed with increasing Ni amount (see fig. S1(b) of the supplemental materials). The change in lattice constants ratio *c*/*a* at room temperature by increasing Ni concentration is shown in fig. S1(c). The *c*/*a* at room temperature for $FeZr_2$ is shown in fig. S1 (d). The *c*/*a* at room temperature correlates to the sign of the coefficient of uniaxial thermal expansion along the *c*-axis[12]. We found that $FeZr_2$ contains impurity phases of Fe_2Zr and Zr, whereas $Co_{1-x}Ni_xZr_2$ ($x=0$, 0.2, 0.4, 0.6, 0.8, 1) were confirmed as almost single-phase quality (see figs. S1(d) and S1(e) of supplemental materials). The actual compositions of the obtained samples were consistent with nominal compositions (see table S1 of Supplemental Materials), which were examined by energy-dispersive X-ray spectroscopy (EDX) method on a scanning electron microscope (SEM) TM-3030plus (Hitachi High-Tech) equipped with detector system SwiftED (Oxford). SEM images and elemental mapping images of $FeZr_2$ and $Co_{0.6}Ni_{0.4}Zr_2$are shown in Figs. S2(a) and S2(b) of the Supplemental Materials, respectively. The schematic images of crystal stricture were depicted using VESTA[22].

Specific heat measurements were performed by thermal relaxation method using a Physical Property Measurement System (PPMS Dynacool, Quantum Design). The samples were fixed on a sample stage with the Apiezon N grease.

Sound velocity measurements were performed using 1077DATA (KARL DEUTSCH), and the longitudinal and transverse sound velocities were separately determined.

Calculation methods

Our calculations have been carried out using density functional theory (DFT) as instated in the Vienna Ab initio Simulation Package (VASP)[23–25]and QUANTUM ESPRESSO package (QE)[26,27]. In VASP, the exchange-correlation energies were considered as described by employing the Perdew, Burke, and Ernzerhof (PBE) functional[28]within the generalized gradient approximation (GGA). Projector-augmented waves (PAWs)[29]were used to represent the electron-ion interactions. A $12\times12\times12$ Monkhorst–Pack k-point[30] mesh was used for structural properties. The convergence criteria for energy and force were 1×10^{-6} and 1×10^{-4}, respectively. The kinetic energy cutoff for plane wave expansion was set to 500 eV. This k-point and energy cutoff were sufficient for obtaining well-converged structural and electronic structure results.

For phonon dispersion curves, the PHONOPY code was used through density functional perturbation theory[31] employing a $4\times4\times4$ supercell approximation. However, to determine the thermal expansion property, it is necessary to perform numerous phonon calculations for lattice parameters optimized at lower and higher values. Thermal expansion was predicted by the quasi-harmonic approximation (QHA). The most conventional approach for calculating thermal expansion based on QHA is directly minimizing the free energy. Here, we utilized machine learning capabilities within VASP to address the high cost associated with these extensive phonon calculations. This facilitated the seamless integration of phonon dispersion analysis into our research workflow. This method highlights the effective combination of machine learning and on-the-fly phonon calculations, offering a robust approach for studying lattice vibrations and enhancing our comprehension of material properties crucial for diverse applications.

The superconductivity properties were also studied utilizing the Quantum ESPRESSO (QE) code[26,27]. For exchange-correlation functional Perdew-Burke-Ernzerhof (PBE) type[28], Generalized Gradient approximations (GGA) and ultrasoft pseudopotentials with scalar relativistic were used. Broyden–Fletcher–Goldfarb–Shanno (BFGS) algorithm[32]was chosen to optimize geometry. The Methfessel–Paxton broadening technique[33] was used with the smearing parameter 0.03 Ry. The kinetic energy cut-off for wave functions and charge density were set to 60 Ry and 480 Ry, respectively. For Brillouin zone integration with a $16\times16\times16$ k-point grid for self-consistent calculations.

The phonon calculations were performed using density functional theory in the linear response approach[26,27]. We calculated electron-phonon coupling starting from a coarse k-point and q-point mesh, followed by interpolation to a finer mesh. Specifically, initial calculations used a 16×16×16 k-point grid and a 4×4×4 uniform grid of q-points was taken for dynamical matrices within the Brillouin zone, which we then refined incrementally. This setup was refined incrementally to a denser mesh, optimizing the balance between computational efficiency and accuracy. These matrices were Fourier-transformed into real space to construct the force constants, allowing for phonon frequency calculations at any selected q-point. These initial grids provided a good balance between computational efficiency and accuracy, allowing us to test convergence by increasing the density until changes in the coupling constant "λ" were minimized. To ensure the reliability of the mesh grids, we monitored the values of the electron-phonon coupling constant "λ" as we increased k- and q-point density. This approach verified that further refinement of the grid would lead to negligible changes in "λ", thereby confirming convergence. The methods for convergence testing were chosen to align with standards set by similar studies, including[34]. The electron-phonon matrix elements were calculated using a combination of the linear response theory[26,27], and the Migdal–Eliashberg theory[35,36]. The calculated electron-phonon coupling strength at each mode λ_{qv} which is given by

$$\lambda_{qv} = \frac{\gamma_{qv}}{\pi\hbar N(E_F)\,\omega_{qv}^2}$$

The Eliashberg spectral function for electron–phonon interaction, represented in terms of phonon line width γ_{qv} is defined as follows:

$$\alpha^2F(\omega) = \frac{1}{2\pi\, N(E_F)} \sum_{qv} \frac{\gamma_{qv}}{\hbar\,\omega_{qv}} \delta(\omega - \omega_{qv})$$

$$\gamma_{qv} = 2\pi\,\omega_{qv} \sum_{kn} \left| g^{qv}_{(k+q)m;kn} \right|^2 \delta(\epsilon_{kn} - \epsilon_F)\delta(\epsilon_{(k+q)n} - \epsilon_F)$$

where, $N(E_F)$ and $g^{qv}_{(k+q)m;kn}$ represent the electronic density of states at the Fermi level and the electron-phonon coupling matrix element, respectively. The electron–phonon matrix elements $g^{qv}_{(k+q)m;kn}$ are calculated self-consistently using linear response theory[26,27]. Once the Eliashberg spectral function is obtained, the electron–phonon coupling constant can be obtained by

$$\lambda = \sum_{qv} \lambda_{qv} = 2\int \frac{\alpha^2F(\omega)}{\omega} \mathrm{d}\omega$$

The logarithmically averaged frequency $\omega_{\log}$ was defined as

$$\omega_{\log} = \exp\left(\frac{2}{\lambda}\int \frac{d\omega}{\omega}\alpha^2F(\omega)\ln\omega\right)$$

where $\alpha^2F(\omega)$ is the Eliashberg phonon spectral function. McMillan's equation, modified by Allen and Dynes[37–39] was applied to estimate the superconducting transition temperature (Tc) as follows:

$$T_c = \frac{\omega_{\log}}{1.20}\exp\left[-\frac{1.04(1+\lambda)}{\lambda - \mu^*(1+0.62\lambda)}\right]$$

where the parameter μ^* indicates effective Coulomb repulsion, with values usually ranging between 0.10 and 0.16.

Data availability

All data are available by reasonable request to corresponding authors.

Received: 30 July 2024; Accepted: 8 November 2024
Published online: 14 November 2024

References

1. Takenaka, K. Negative thermal expansion materials: technological key for control of thermal expansion. *Sci. Technol. Adv. Mater.* **13**, 013001 (2012).
2. Mary, T. A., Evans, J. S. O., Vogt, T. & Sleight, A. W. Negative thermal expansion from 0.3 to 1050 Kelvin in ZrW_2O_8. *Science*. **272**, 90–92 (1996).
3. Ramirez, A. P. & Kowach, G. R. Large low temperature specific heat in the negative thermal expansion compound ZrW_2O_8. *Phys. Rev. Lett.* **80**, 4903–4906 (1998).
4. Ernst, G., Broholm, C., Kowach, G. R. & Ramirez, A. P. Phonon density of states and negative thermal expansion in ZrW_2O_8. *Nature*. **396**, 147–149 (1998).
5. Pryde, A. K. A. et al. Rigid unit modes and the negative thermal expansion in ZrW_2O_8. *Phase Transit.* **61**, 141–153 (1997).
6. Takenaka, K. & Takagi, H. Magnetovolume Effect and Negative Thermal Expansion in $Mn_3(Cu_{1-x}Ge_x)N$. *Mater. Trans.* **47**, 471–474 (2006).
7. Kobayashi, M. & Mochizuki, M. Theory of magnetism-driven negative thermal expansion in inverse perovskite antiferromagnets. *Phys. Rev. Mater.* **3**, 024407 (2019).

8. Chen, J., Hu, L., Deng, J. & Xing, X. Negative thermal expansion in functional materials: controllable thermal expansion by chemical modifications. *Chem. Soc. Rev.* **44**, 3522–3567 (2015).
9. Fujishita, H. et al. X-ray diffraction study of spontaneous strain in Fe-pnictide superconductor, $NdFeAsO_{0.89}F_{0.11}$. *Eur. Phys. J. B.* **85**, 52 (2012).
10. Mizuguchi, Y., Kasem, M. R. & Ikeda, Y. Anomalous thermal expansion in a $CuAl_2$-type Superconductor $CoZr_2$. *J. Phys. Soc. Jpn.* **91**, 103601 (2022).
11. Watanabe, Y., Arima, H., Usui, H. & Mizuguchi, Y. Sign change in *c*-axis thermal expansion constant and lattice collapse by Ni substitution in transition-metal zirconide superconductor $Co_{1-x}Ni_xZr_2$. *Sci. Rep.* **13**, 1008 (2023).
12. Arima, H., Kasem, M. R. & Mizuguchi, Y. Axis thermal expansion switching in transition-metal zirconides $TrZr_2$ by tuning the *c*/*a* ratio. *Appl. Phys. Express.* **16**, 035503 (2023).
13. Ryazanov, V. V. et al. Magnetic Josephson Junction Technology for Digital and Memory Applications. *Phys. Procedia*. **36**, 35–41 (2012).
14. Xu, M. et al. Giant uniaxial negative thermal expansion in $FeZr_2$ alloy over a wide temperature range. *Nat. Commun.* **14**, 4439 (2023).
15. Teruya, A. et al. Superconducting and Fermi Surface Properties of single crystal Zr_2Co. *J. Phys. Soc. Jpn*. **85**, 034706 (2016).
16. Kasem, M. R. et al. Anomalous broadening of specific heat jump at Tc in high-entropy-alloy-type superconductor $TrZr_2$. *Supercond Sci. Technol.* **34**, 125001 (2021).
17. Bonhomme, F., Yvon, K. & Zolliker, M. Tetragonal Zr_2CoD_5 with filled Al_2Cu-type structure and ordered deuterium distribution. *J. Alloys Compd.* **199**, 129–132 (1993).
18. McCarthy, S. L. The superconductivity and magnetic susceptibility of some zirconium-transition-metal compounds; evidence for an anticorrelation. *J. Low Temp. Phys.* **4**, 489–501 (1971).
19. Matthias, B. T. & Corenzwit, E. Superconductivity of Zirconium alloys. *Phys. Rev.* **100**, 626–627 (1955).
20. Havinga, E. E., Damsma, H. & Hokkeling, P. Compounds and pseudo-binary alloys with the $CuAl_2$(C16)-type structure I. Preparation and X-ray results. *J. Less Common. Met.* **27**, 169–186 (1972).
21. Izumi, F. & Momma, K. Three-Dimensional visualization in Powder Diffraction. *Solid State Phenom.* **130**, 15–20 (2007).
22. Momma, K. & Izumi, F. VESTA 3 for three-dimensional visualization of crystal, volumetric and morphology data. *J. Appl. Crystallogr.* **44**, 1272–1276 (2011).
23. Kresse, G. & Furthmüller, J. Efficient iterative schemes for ab initio total-energy calculations using a plane-wave basis set. *Phys. Rev. B.* **54**, 11169–11186 (1996).
24. Kresse, G. & Furthmüller, J. Efficiency of ab-initio total energy calculations for metals and semiconductors using a plane-wave basis set. *Comput. Mater. Sci.* **6**, 15–50 (1996).
25. Kresse, G. & Hafner, J. Ab initio molecular dynamics for liquid metals. *Phys. Rev. B.* **47**, 558–561 (1993).
26. Giannozzi, P. et al. QUANTUM ESPRESSO: a modular and open-source software project for quantum simulations of materials. *J. Phys. Condens. Matter.* **21**, 395502 (2009).
27. Giannozzi, P. et al. Advanced capabilities for materials modelling with Quantum ESPRESSO. *J. Phys. Condens. Matter.* **29**, 465901 (2017).
28. Perdew, J. P., Burke, K. & Ernzerhof, M. Generalized gradient approximation made simple. *Phys. Rev. Lett.* **77**, 3865–3868 (1996).
29. Blöchl, P. E. Projector augmented-wave method. *Phys. Rev. B.* **50**, 17953–17979 (1994).
30. Monkhorst, H. J. & Pack, J. D. Special points for Brillouin-Zone integrations. *Phys. Rev. B.* **13**, 5188–5192 (1976).
31. Togo, A., Oba, F. & Tanaka, I. First-principles calculations of the ferroelastic transition between rutile-type and $CaCl_2$-type SiO_2 at high pressures. *Phys. Rev. B.* **78**, 134106 (2008).
32. Fischer, T. H. & Almlof, J. General methods for geometry and wave function optimization. *J. Phys. Chem.* **96**, 9768–9774 (1992).
33. Methfessel, M. & Paxton, A. T. High-precision sampling for Brillouin-Zone integration in metals. *Phys. Rev. B.* **40**, 3616–3621 (1989).
34. Tong, Z., Li, S., Ruan, X. & Bao, H. Comprehensive first-principles analysis of phonon thermal conductivity and electron-phonon coupling in different metals. *Phys. Rev. B.* **100**, 144306 (2019).
35. Migdal, A. B. Interaction between electrons and lattice vibrations in a normal metal. *Sov Phys. JETP*. **7**, 996 (1958).
36. Eliashberg, G. M. Interactions between electrons and lattice vibrations in a superconductor. *Sov Phys. JETP*. **11**, 696 (1960).
37. McMillan, W. L. Transition temperature of strong-coupled superconductors. *Phys. Rev.* **167**, 331–344 (1968).
38. Allen, P. B. & Dynes, R. C. Transition temperature of strong-coupled superconductors reanalyzed. *Phys. Rev. B.* **12**, 905–922 (1975).
39. Allen, P. B. & Dynes, R. C. Superconductivity at very strong coupling. *J. Phys. C: Solid State Phys.* **8**, L158 (1975).

Acknowledgements

The authors thank O. Miura and T. Shiga for their support in experiments and discussion. This work is partly supported by JSPS-KAKENHI (grant NO. 23KK0088), JST-ERATO (grant NO. JPMJER2201), TMU Research Project for Emergent Future Society, and Collaborative Research Project of Laboratory for Materials and Structures, Institute of Innovative Research, Tokyo Institute of Technology. This study was computationally supported by T.C. Strategy and Budget Directorate under Project No: 2019K12-92587.

Author contributions

Y.W. and Y.M. designed the research. Y.W., M. R. K, A.Y., and T.K conducted the experiment(s). Y.W. and Y.M. analyzed the results. C.T. and M.Ç. conducted theoretical calculation(s). All authors reviewed the manuscript.

Declarations

Competing interests

The authors declare no competing interests.

Additional information

Supplementary Information The online version contains supplementary material available at https://doi.org/10.1038/s41598-024-79353-8.

Correspondence and requests for materials should be addressed to C.T. or Y.M.

Reprints and permissions information is available at www.nature.com/reprints.

Publisher's note Springer Nature remains neutral with regard to jurisdictional claims in published maps and institutional affiliations.

Open Access This article is licensed under a Creative Commons Attribution-NonCommercial-NoDerivatives 4.0 International License, which permits any non-commercial use, sharing, distribution and reproduction in any medium or format, as long as you give appropriate credit to the original author(s) and the source, provide a link to the Creative Commons licence, and indicate if you modified the licensed material. You do not have permission under this licence to share adapted material derived from this article or parts of it. The images or other third party material in this article are included in the article's Creative Commons licence, unless indicated otherwise in a credit line to the material. If material is not included in the article's Creative Commons licence and your intended use is not permitted by statutory regulation or exceeds the permitted use, you will need to obtain permission directly from the copyright holder. To view a copy of this licence, visit http://creativecommons.org/licenses/by-nc-nd/4.0/.

© The Author(s) 2024